Image Performance Characterization of an In-Beam Low-Field Magnetic Resonance Imaging Systemm During Static Proton Beam Irradiation

Gantz, S.; Schellhammer, S.; Hoffmann, A. L.;

Originally published:

June 2021

IEEE Transactions on Radiation and Plasma Medical Sciences 6(2022)3, 271-281

DOI: https://doi.org/10.1109/TRPMS.2021.3085991

Perma-Link to Publication Repository of HZDR:

https://www.hzdr.de/publications/Publ-31673

Image Performance Characterization of an *In-Beam* Low-Field Magnetic Resonance Imaging System During Static Proton Beam Irradiation

Sebastian Gantz, Sonja M. Schellhammer, and Aswin L. Hoffmann

***Abstract*—Image guidance using *in-beam* real-time magnetic resonance (MR) imaging is expected to improve the targeting accuracy of proton therapy for moving tumors, by reducing treatment margins, detecting inter- and intrafractional anatomical changes and enabling beam gating. The aim of this study was to quantitatively characterize the static magnetic field and image quality of a 0.22 T open MR scanner that has been integrated with a static proton research beamline. The magnetic field and image quality studies were performed using high-precision magnetometry and standardized diagnostic image quality assessment protocols, respectively. The magnetic field homogeneity was found to be typical of the scanner used (98 ppm). Operation of the beamline magnets changed the central resonance frequency and magnetic field homogeneity by a maximum of 16 Hz and 3 ppm, respectively. It was shown that the *in-beam* MR scanner features sufficient image quality and influences of simultaneous irradiation on the images are restricted to a small sequence-dependent image translation and a minor reduction in signal-to-noise ratio. Nevertheless, specific measures have to be taken to minimize these effects in order to achieve accurate and reproducible imaging which is required for a future clinical application of MR integrated proton therapy.**

***Index Terms*—MRI, proton therapy, image quality, magnetometry, MR guided radiotherapy.**

I. Introduction

In most clinical proton therapy (PT) centers the patient setup for treatment is to date still based on orthogonal X-ray imaging. While some centers have advanced to image guidance based on in-room computer tomography (CT) or on-board cone-beam CT, which at least allows for monitoring of anatomical changes between treatment fractions, these modalities offer limited soft-tissue contrast and expose healthy normal tissue to ionising radiation dose. For the treatment of mobile soft-tissue tumors, high-contrast real-time imaging is required for online beam gating or tumor tracking. In photon therapy (XT), such real-time image guidance is realised by magnetic resonance (MR) guided linear accelerator systems (MRXT). Currently two such commercially available systems have been introduced into the clinic [1], [2] and further groups are developing independent prototype systems [3], [4]. However, due to the much steeper dose gradient and increased sensitivity to anatomical variations and organ motion of PT, online image guidance in PT is expected to be even more important than for XT, especially regarding moving soft-tissue tumors [5]. Despite this strong motivation, the development of MR-integrated proton therapy (MRiPT) is still in its infancy, due to a number of unresolved technological questions [6]. One of the key aspects highlighted by Hoffmann et al. [6] is the electromagnetic interference between the PT system and the MR imager. The MR image quality is expected to be influenced by the presence and operation of the PT system, mainly due to the magnetic fringe fields of the beamline magnets that are expected to overlap with the imaging magnetic field of the MR scanner and thus result in a degradation of image quality.

In 2018, we have shown for the first time that an 0.22 T open MR scanner designed for musculoskeletal imaging (MrJ 2200, ASG Superconductors S.p.A., Genoa, Italy) can been integrated with a horizontal static research proton beamline [7]. The study by Schellhammer et al. [7] included the setup, beam alignment, beam quality and first anatomical images with this *in-beam* MR research setup, thus proving the feasibility of simultaneous imaging during proton beam irradiation. However, a comprehensive quantitative analysis of image quality is missing in this work. Such an analysis is important since it allows to investigate in detail any beam related effects on the image quality of the scanner and it is the basis for the definition of a quality assurance (QA) protocol for future MRiPT systems to be used for patient treatment, to assure reproducible and accurate images. As shown in [8] for the first MRXT system, image QA regarding an *in-beam* MR system for radiation therapy requires additional parameters to be studied as compared to diagnostic MR systems, such as signal-to-noise ratio (SNR) and geometric fidelity. As the MRI system studied here utilizes a permanent magnet design which is known to show a residual temperature induced frequency drift, absolute positioning of the image is a further crucial parameter, as MR images shall be used for patient positioning and treatment adaptation, thus absolute geometric accuracy is of paramount importance. Therefore, the aim of the current study is twofold. Firstly, for the field strength and homogeneity of the main magnetic field of the MR scanner (B_0), effects

S. Gantz, S. M. Schellhammer and A. L. Hoffmann are with OncoRay – National Center for Radiation Research in Oncology, Faculty of Medicine and University Hospital Carl Gustav Carus, Technische Universität Dresden, Helmholtz-Zentrum Dresden-Rossendorf, Dresden, Germany

S. Gantz, S. M. Schellhammer and A. Hoffmann are with Institute of Radiooncology-OncoRay, Helmholtz-Zentrum Dresden-Rossendorf, Dresden, Germany

A.Hoffmann is with Department of Radiotherapy and Radiation Oncology, Faculty of Medicine and University Hospital Carl Gustav Carus, Technische Universität Dresden, Dresden, Germany

S.Gantz and S.Schellhammer contributed equally to this work

Manuscript received XX YY, 2020

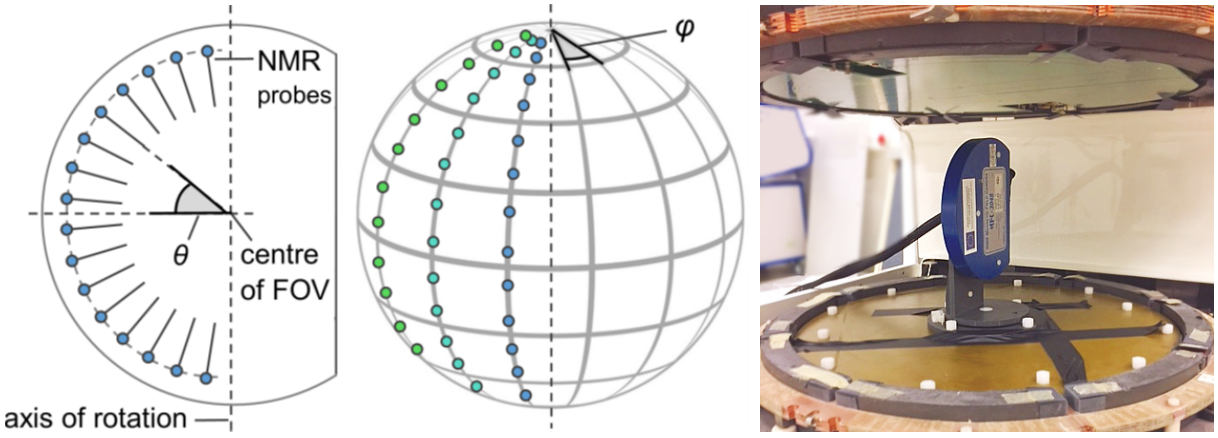

(a) (b) (c)

Fig. 1. (a) Schematic representation of the half-moon shaped magnetic field camera with 16 individual NMR probes, distributed along the polar angle θ. (b) Schematic representation of the measurement locations of a 16 × 12 samples B_0 field map on the surface of a 22 cm diameter spherical volume. The azimuthal angle ϕ denotes the camera position (ϕ = 0° when camera looking away from the beam exit window). (c) Setup of the camera at the magnetic isocenter of the MR scanner.

of temperature change and energizing the beamline magnets of the PT system are studied. Secondly, regarding the image quality of the scanner, we compare two scenarios, imaging with and without simultaneous proton beam irradiation by a quantitative assessment of: (1) the ACR (American College of Radiology) phantom test, (2) the SNR test, and (3) the absolute positional accuracy test.

II. Material and Methods

A. Measurement Setup

This study uses the exact same setup as reported in [7]. The C-shaped open MR scanner based on a 0.22 T permanent magnet utilized a vertically upwards directed B_0 field and was positioned in front of a fixed horizontal proton research beamline, with the beam-exit window, last pair of focussing quadrupole magnets and 30° bending magnet at a distance of 1.1 m, 2.8 m and 7.1 m stream upwards from the MR magnetic isocenter, respectively.

B. Magnetic Field Strength and Homogeneity

The static magnetic field around the MR magnetic isocenter was mapped using a half-moon shaped magnetic field camera (MFC 3048, MetroLab, Geneva, Switzerland) containing 16 NMR probes evenly distributed along the arc of the half circle (Fig. 1). Each probe measured the resonance frequency at a specific location. The probe array was vertically mounted on a manually rotatable holder with its origin aligned with the magnetic isocenter of the MR scanner. The probe array was either directed towards the beam exit window at a fixed azimuthal angle of ϕ = 180° or manually rotated over 360° along the B_0 field axis at 12 equidistant azimuthal angles of 30° each. In the former case, in total 16 samples were acquired on the arc with a radius of 11 cm, whereas in the latter case, for a full rotation, in total 16 × 12 samples were acquired on the surface of a 22 cm diameter-spherical volume (DSV). From this data, both the central resonance frequency (f_n), which was the average frequency over all n samples, and the peak-to-peak frequency variation relative to the central resonance frequency to indicate the magnetic field homogeneity (MFH_n) were calculated.

1) Magnetic Field Drift: Since the MR scanner is based on biplanar permanent magnets made of $Nd_2Fe_{14}B$ material, it is known to be very sensitive to temperature fluctuations [9]. The temperature coefficient of the residual magnetic flux density of $Nd_2Fe_{14}B$ is about -1100 ppm·K^{-1} [10]. To compensate for thermal drift effects of the B_0 field the magnets and the steel flux return yoke are temperature controlled at 36.0 °C. The temperature stability, as measured by the internal temperature sensors of the MR scanner, is better than 0.3 mK. However, this measure provides no information on the temperature distribution over the whole volume of the magnet and given the very low thermal conductivity of the $Nd_2Fe_{14}B$ of 7-8 W (m·K)$^{-1}$ [10], the B_0 field strength and homogeneity of the scanner are expected to exhibit a residual drift due to environmental temperature fluctuations [11]. To evaluate the magnitude and rate of this drift long-term measurements over 4 days (with a 2-hour break during the second day for reference rotation measurements, see below) were performed with the magnetic field camera positioned at a fixed azimuthal angle of ϕ = 180° and a sampling rate of 0.1 Hz, yielding a time series of f_{16} and MFH_{16}. To be able to correlate the frequency drift with the ambient temperature, T_a, the room temperature was logged with a SL52T (Signatrol, Tewkesbury, UK) miniature temperature data logger positioned at the outside wall of the Faraday cage at a sampling rate of 2 minutes. The correlation between f_{16}, MFH_{16} and T_a was determined by the Pearson correlation coefficient. During the 2-hours break on day 2, three full rotations of the magnetic field camera were performed to measure the MFH_{192} and f_{192}. For these rotation measurements, it was assured that all beamline magnets were switched off.

2) Effect of Beamline Magnets: The magnetic fringe fields produced by the beamline magnets are expected to overlap with the magnetic field deployed for imaging by the *in-*

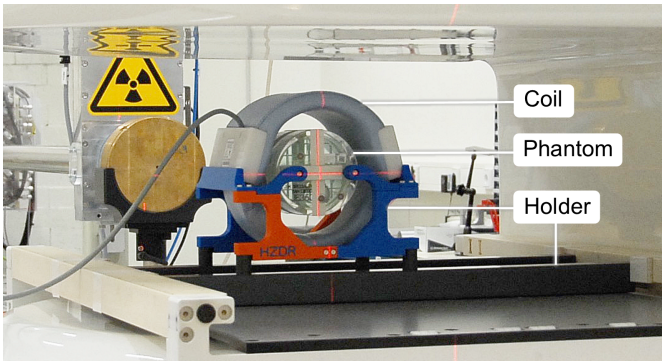

Fig. 2. The ACR Small phantom placed inside the knee coil, the holder and the MR scanner in front of the beam exit. Top part of the Faraday cage was removed for this photo.

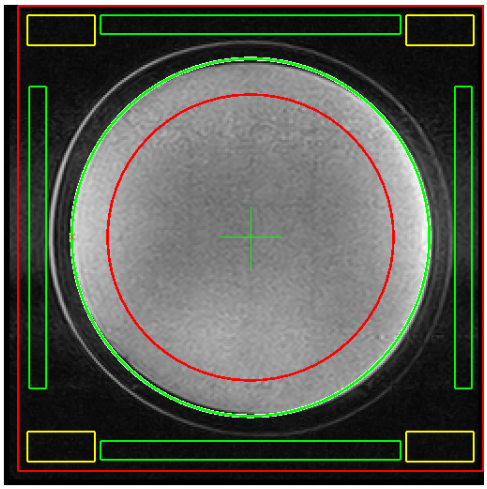

Fig. 3. : Image analysis on slice 4 of the T_2^*-weighted GE sequence, showing regions of interest used for the SNR test (red circle and yellow rectangles), the ghosting test (green rectangles), and the phantom center determination (green circle and cross).

beam MR scanner and hence distort the B_0 field, which will potentially compromise the MR image quality. To study this effect, the B_0 field was mapped with the beamline magnets being energized for nominal proton energies in the clinical range of $75 - 225$ MeV at equidistant energy steps of 25 MeV. For each beam energy one full rotational measurement by the MFC was acquired with baseline measurements using non-energized beamline magnets in between, to compensate for the magnetic field drift that may occur due to environmental temperature changes, through a linear relationship. For the beamline settings at 125 MeV two additional full rotations were performed, to measure the reproducibility and the robustness of the drift rate correction.

C. MR Image Quality

1) Imaging Protocol: For the MR imaging experiments, the ACR Small Phantom was placed centrally inside a dedicated knee coil, which were both positioned reproducibly in the magnetic isocenter using an in-house built phantom holder (Fig. 2). As shown with EBT3 film by [7] a 2 cm lateral displacement of the MR scanner relative to the beam central axis assured that a 125 MeV proton beam centrally impinged on the phantom's front face. Following the ACR Small Phantom protocol [12], a sagittal locator scan and a set of seven axial T_1- and T_2-weighted spin echo (SE) images were acquired for each measurement (see Table I). Since gradient echo (GE) sequences are commonly used for real-time imaging and are more sensitive to magnetic field inhomogeneity [13] than SE sequences, two GE scans were added to the protocol, with seven axial slices each: first, a fast T_1-weighted GE sequence using the shortest achievable repetition time of the MR scanner, and second, a magnetic field-sensitive T_2^*-weighted GE sequence using the highest achievable echo time. A subsequent acquisition of the locator and the four SE and GE sequences is called 'imaging set' in the following. To separate statistical fluctuations from systematic differences in the image quality, 24 imaging sets were acquired each with (a) all beamline magnets switched off and (b) during simultaneous proton beam irradiation. Image sets with and without irradiation were acquired alternately to minimise the influence of possible temporal dependencies such as the temperature induced B_0 drift (section III-A1). The beam energy (125 MeV) was chosen such that the beam traversed all axial imaging planes and stopped at the distal region of the phantom behind the last imaging plane. This energy was calculated by a simple Geant4 Monte Carlo simulation of monoenergetic, parallel proton pencil beams of different energies through a simplified water phantom without inner structures. The beam current was set to the maximum (5.4 nA at beam exit window) to gain a worst-case estimate of any beam-related effects. Before each imaging set, a calibration of the transmission frequency was performed and a Scout scan, i.e. a set of three orthogonal SE localizer images, was acquired with the beamline magnets switched off. On the Scout scan, the position of the imaging slices in the phantom was visually verified according to the ACR Phantom test protocol.

2) Image Quality Parameters: For diagnostic MR system quality assurance, a periodic control of the geometric accuracy, slice-position and -thickness accuracy, high contrast spatial resolution, low contrast detectability, image intensity uniformity and percentage signal ghosting parameters as defined by the ACR [12], is the gold standard. As described by [8] MR quality assurance for radiotherapy purposes requires the evaluation of additional parameters. Thus, the image SNR was deduced in accordance with the NEMA standard MS-1 from the mean phantom fluid signal and the standard deviation of the signal in a region outside of the phantom [14], [15]. Regions of interest (ROI) for both signal and noise are indicated in red and yellow in Fig. 3, respectively. Additionally, since a uniform phantom shift along frequency encoding direction (FE) was expected [7] as a result of changes in B_0 due to the overlapping fringe fields of the beamline magnets, the absolute position of the phantom center in both frequency and phase encoding (PE) direction was analysed. The phantom center was determined using a Hough transform [16] (green circle in Fig. 3), yielding the center coordinates of the fitted circle (green cross in Fig. 3) relative to the center of the image with the coordinate axis pointing down and right. This analysis

TABLE I
MR SEQUENCE PARAMETERS FOR THE IMAGE QUALITY TESTS. PARAMETERS MARKED WITH ASTERISK (*) DEVIATE FROM THE ACR PROTOCOL DUE TO LIMITATIONS OF THE MR SCANNER. THE GE SEQUENCES WERE ADDED TO THE ACR PROTOCOL FOR THIS STUDY.

Sequence	Scout	Locator	T_1 SE	T_2 SE	T_1 GE	T_2^* GE
FOV diameter / cm	26	12	12	12	12	12
Number of slices	1	1	7	7	7	7
Interslice space / mm	-	-	3	3	3	3
Slice thickness / mm	8	10*	5	5	5	5
Matrix size	(160,128)	(192,152)	(192,152)	(192,152)	(192,152)	(192,152)
Number of excitations	1	1	1	1	1	1
Echo time / ms	18	20	20	28*,93*	8	30
Repetition time / ms	100	200	500	2000	30	80
Flip angle / (°)	90	90	90	90	20	20
Acquisition time (min:s)	0:18	0:35	1:21	3:01	1:10	1:52

additionally allowed to study the system robustness against mean frequency drift and thus the stability of the transmission frequency calibration.

3) Parameter Analysis and Statistical Testing: Image parameters were semi-automatically evaluated on the 256 × 256 DICOM images reconstructed by the manufacturer provided MR software, using the in-house developed and internally validated AMRIQA software tool [15]. A detailed description of the image parameter acquisition from the image slices 1–7 can be found in literature [14], [17] and in the ACR Small Phantom protocol [12]. For the evaluation of the SNR and absolute phantom position, the software was extended for this study by implementing a circular Hough transform [16] in slice 4. The automated analysis was supervised visually to detect any implausible results. Two parameters, the slice thickness and the low-contrast detectability, were found to be not reliably quantified by the software due to the low SNR of the MR images. These were therefore evaluated manually according to the ACR Small Phantom protocol [12]. The median and interquartile range of all 13 image quality parameters and 5 sequences were calculated for the images acquired with and without simultaneous irradiation. As a first external reference, these results were compared to the minimum performance thresholds as defined by the "Recommended Action Criteria" of the ACR [12]. It should be noted, however, that these criteria are commonly used for the diagnostic application of high-field 1.5 T scanners, which are known to have a higher SNR in comparison to a 0.22 T scanner. As far as we know, no established criteria exist for low-field MR scanners and their application in radiotherapy. To test the hypothesis that the image quality with and without simultaneous irradiation was equivalent, a TOST (two one-sided test) equivalence test [18], [19] was applied for all image quality parameters and sequences. Since no minimum performance thresholds had been established so far, the equivalence margins were based on the phantom and image-specific discretisation: one pixel width for the geometrical parameters (i.e. 0.47 mm along PE and FE direction and 5 mm along slice encoding direction), two spokes for the low-contrast object detectability, 0.1 mm for the resolution, and 10 % of the median for the SNR, image uniformity, and ghosting ratio. As the statistical analysis of this amount of parameters (12 × 4 + 1 = 49) would yield an unacceptable amount of random false-positives, a Bonferroni-

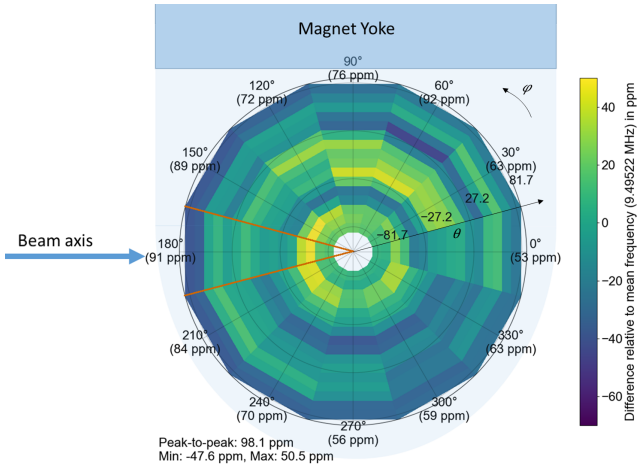

Fig. 4. Polar plot of the 3D magnetic field map of the MR scanner superimposed onto a top-view of the MRI scanner with the 192 measurement points on a 22 cm DSV. Angular component denotes camera position ($\phi = 0°$ equals position 1). Radial component of the plot denotes the individual NMR probes, South pole in the center, North pole at the rim. The beam axis was added for better understanding of the geometrical position. Distances are not to scale. MFH_{16} values for the individual angular measurements are given in brackets.

Holm correction [20] was applied to achieve a family-wise false positive error rate of $\alpha = 5$ %. An image quality parameter was considered equivalent if the corresponding equivalence test was significant. Otherwise, the statistical difference in the parameter was tested by an inferiority t-test with a significance level of $\alpha = 5$ %. Since the parameter distributions were monomodal and fairly symmetric, a normal distribution was assumed for the statistical tests.

III. RESULTS

A. Magnetic Field Measurements

1) Temperature induced B_0 Drift and Reference Measurement: For the long-time thermal drift measurement, the mean resonance frequency f_{16} was found to oscillate with a periodicity of about 24 h, with a maximum absolute slope of about 15 Hz/h and an amplitude of about 60 Hz, see Fig. A.1. Given the temperature coefficient of the residual magnetic flux density of the magnets material -0.1 % / K [10], this translates to a temperature change on the order of 10 mK inside the permanent magnet material. Ambient temperature

TABLE II
CHANGE IN MEAN RESONANCE FREQUENCY (Δf_{192}) AS FUNCTION OF SETTING THE BEAMLINE MAGNETS TO DIFFERENT PROTON ENERGIES.

Energy [MeV]	75	100	125	150	175	200	225
Δf_{192} [Hz]	-13 ± 1	-15 ± 1	-15 ± 1	-16 ± 1	-16 ± 1	-11 ± 1	+7 ± 1

T_a measurements showed changes in the range of 23.7 – 24.2 °C over the course of the experiment. The temperature T_a and frequency f_{16} were negatively correlated with p = -0.62. The MFH_{16} exhibited an oscillating behaviour, positively correlated (p = 0.95) with the frequency f_{16}, with the same 24 h periodicity and an amplitude of about 1.5 ppm. For the three rotations under reference conditions, with the beamline magnets switched off, the MFH_{192} was 98.1, 97.9 and 98.2 ppm (Fig. 4). Point-wise absolute differences of all 192 probes for the three measurements were within 2.1 ppm. The mean and standard deviation of f_{192} for the three measurements was 9495219.0 ± 1.7 Hz.

2) Effect of the Proton Beamline: The change in mean resonance frequency, Δf_{192}, as a function of proton beam energy is shown in Table II. A marked beam energy dependent change in Δf_{192} is observed, with the mean frequency decreasing for all energies between 75 MeV and 200 MeV and increasing for 225 MeV. For all measurements, no relevant changes in MFH_{192} were seen, with maximum point-wise differences below 2.5 ppm as compared to reference.

B. Image Quality with the Beamline Switched Off

For all studied sequences, MR images were successfully acquired and reconstructed without distortion correction or uniformity enhancement. Figure 5 presents the sagittal localizer and slices 1, 3, 4 and 7 of the T_1-weighted SE images, which are the four slices used for image analysis. Apart from the T_1-weighted GE sequence images, which exhibited radiofrequency spikes and a low signal intensity, all images were artefact free and present a typical image quality for the 0.22 T scanner. The image quality parameters measured with and without simultaneous irradiation for the T_1- and T_2-weighted SE sequence, the T_1- and T_2^*-weighted GE sequence and the locator sequence, are given in the Tables B.1 to B.5 of the Appendix, respectively.

1) ACR Image Quality and SNR: The geometrical image quality parameters showed very good agreement with the ACR Recommended Action Criteria. The axial geometric accuracy, slice position accuracy, and high contrast spatial resolution tests were passed by all four axial sequences, and the sagittal geometric accuracy test was passed by the sagittal locator sequence. As common for low-field MR scanners, the median SNR of the images was low, especially for the T_1 weighted GE sequence (45, 47, 14 and 53 for the T_1- and T_2-weighted SE and the T_1- and T_2^*-weighted GE sequences, respectively). This resulted in a relatively low image intensity uniformity, a high percentage signal ghosting, and a small low-contrast object detectability in comparison to the ACR Recommended Action Criteria. Consequently, the image intensity uniformity test failed for all sequences. The percentage signal ghosting test failed for all sequences except for the T_1-weighted GE sequence. The low-contrast detectability test failed for the GE sequences and only partly passed for the SE sequences. As signal noise obscured the slice thickness test bars, the slice thickness accuracy test failed for the T_1-weighted SE and T_2^*-weighted GE sequences and was not feasible for the T_1-weighted GE sequence. It was only passed by the T_2-weighted SE sequence.

2) Absolute Phantom Position Accuracy: The median absolute position of the phantom center, in both horizontal (i.e. phase encoding) and vertical (i.e. frequency encoding) direction, agreed between the four sequences within 0.4 mm. For the horizontal direction, a systematic median offset of 1.6 mm from the center of the image was observed for all sequences (Fig. 6). The variability of the phantom center in vertical direction was found to be sequence dependent, with an interquartile range from 0.3 to 1.5 mm, and a maximum deviation from 1.3 to 3.6 mm (Fig. 6). Both the interquartile range and maximum deviation increased with decreasing gradient amplitude of the sequences, which was 2.6 mT/m, 1.5 mT/m, 5.7 mT/m and 0.7 mT/m for the T_1- and T_2-weighted SE and the T_1- and T_2^*-weighted GE sequences, respectively. Figure 7 shows an example of this vertical shift between two T_2^*-weighted GE images. For the horizontal direction, however, the variability was smaller and no sequence dependence was observed (see Fig. 6). The interquartile range was between 0.4 and 0.5 mm (i.e. one pixel) for all sequences.

C. Image Quality During Irradiation

For most image quality parameters, the results with and without simultaneous irradiation were statistically equivalent (see Tables B.1 to B.5). However, four parameters were not statistically equivalent for all sequences. Firstly, the absolute vertical position of the phantom center showed a sequence dependent median shift in the opposite direction of frequency encoding of 0.3 mm, < 0.1 mm, 0.2 mm and 0.7 mm for T_1 and T_2-weighted SE and T_1- and T_2^*-weighted GE sequences, respectively (Fig. 8). The inferiority test showed that the decrease in the vertical phantom position with and without simultaneous irradiation was significant for the T_1-weighted SE and the T_1- and T_2^*-weighted GE sequences (with p = 0.04, p = 0.01 and p = 0.04, respectively). Secondly, the SNR was not statistically equivalent for all sequences. A decrease in SNR was observed for all sequences during proton irradiation with a difference of medians of 0.6, 0.9, 0.8 and 1.5 for the T_1- and T_2-weighted SE and the T_1- and T_2^*-weighted GE sequences, respectively (see Tables B.1 to B.4). This decrease was statistically significant for the T_1- and T_2-weighted SE and the T_2^*-weighted GE sequences (with p = 0.01, p = 0.01 and p = 0.02, respectively). Thirdly, the phantom diameter in slice 3 of the T_2^*-weighted GE sequence showed no statistical equivalence. Here, no consistent trend was observed amongst

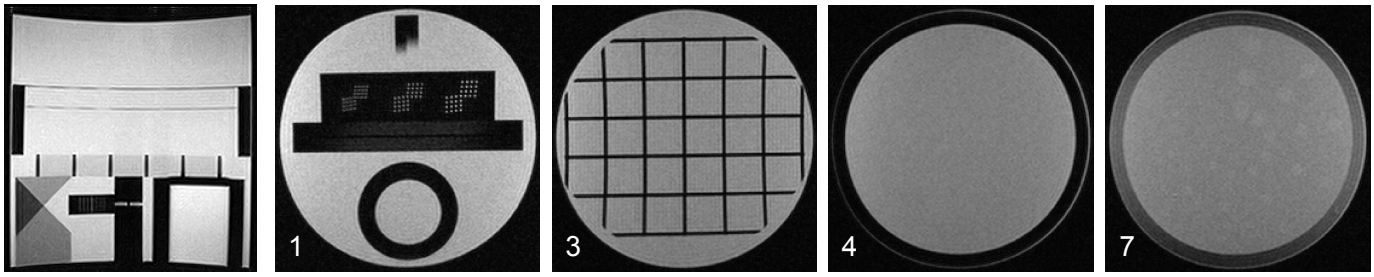

(a) (b) (c) (d) (e)

Fig. 5. T_1-weighted SE MR images of the ACR Small Phantom used for image quality analysis: (a) sagittal locator, (b)-(e) axial slices, with slice number in the bottom left.

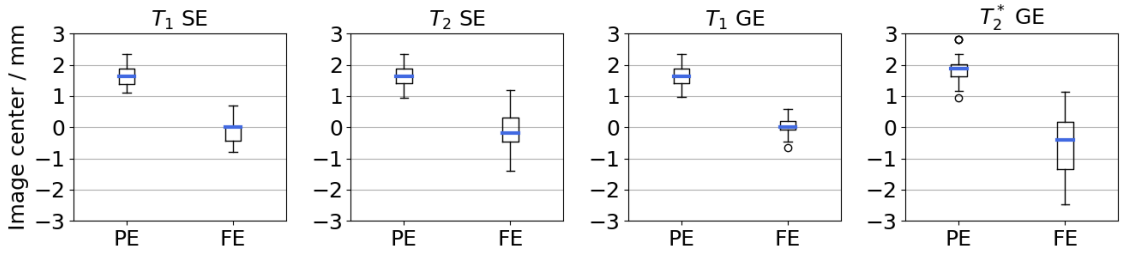

Fig. 6. Measured positions of the phantom center in PE (horizontal) and FE (vertical) direction in MR images for the four different sequences, acquired with the beamline magnets off.

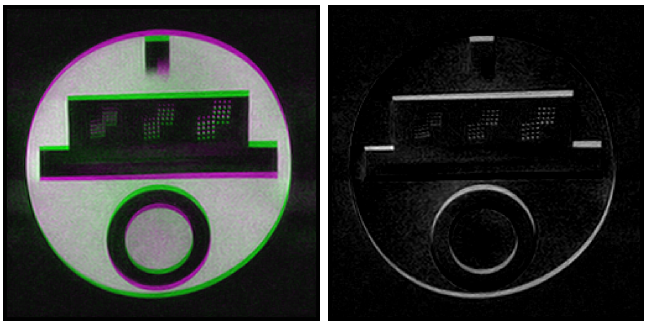

(a) (b)

Fig. 7. Example for the observed image shift along the vertical (frequency-encoding) direction between two subsequently acquired T_2^*-weighted GE images in slice 1. (a) Composite image showing both images overlaid in complementary color bands. (b) Difference image between both images.

the sequences. A high fluctuation was observed as compared to the other sequences, and consequently the inferiority test was not significant. Fourthly, the percentage signal ghosting ratio showed no statistical equivalence for two out of the four sequences. For all sequences, the median differences were below 0.6%. Both SE sequences showed an increase in ghosting whereas for the GE sequences the ghosting ratio showed a minor decrease. The inferiority test was not significant.

IV. Discussion

For hybrid MR-image guided radiation therapy (MR-IGRT) systems the characterization of the imaging performance is an essential part of a QA program to characterize, accept and commission the integrated MRI unit. MR imaging performance characterization studies have been conducted for clinical MR-IGRT systems based on ACR, NEMA and vendor specifications to establish procedures and baseline values for future routine QA [8], [21], [22]. A recent development is the initiation of studies on the technical feasibility to integrate real-time MR imaging and proton therapy [5], [6]. Here, the motivation is that proton therapy is expected to benefit even more from online MR-guidance than photon therapy, since the targeting precision in proton therapy is more challenging than in photon therapy due to the sensitivity of protons to morphological variations (e.g. organ motion and deformation) and patient setup inaccuracies. Although the integration of on-board MR imaging and proton therapy is still in its infancy, a first research prototype system developed by our group made it possible to conduct an initial image performance characterization study. In this work, we quantitatively characterized the image quality of an *in-beam* MR scanner during operation of a static proton research beamline and investigated the influence of the magnetic fringe fields produced by the beamline onto the B_0 field of the MR scanner. Our B_0 field measurements over a 22 cm DSV have shown that the peak-to-peak homogeneity of 98 ppm is within the operating specifications of the low-field open MR scanner used in this study. Although this value is higher than the typical specification of $\sim$2 ppm for superconducting closed-bore high-field diagnostic MRI systems, it is sufficient for the purpose of prototyping an MRiPT system. High B_0 field homogeneity is required for fat suppression, phase-based imaging, spectroscopy and echo-planar imaging type of pulse sequences. As SE based sequences show a relatively small sensitivity to B_0 field perturbations, an acceptable image quality can still be achieved with inhomogeneities of several 10s of ppm [23], [24]. In addition, the B_0 field measurements showed two external sources perturbating the MR imager's central resonance frequency (f_0). Firstly, a residual daily magnetic

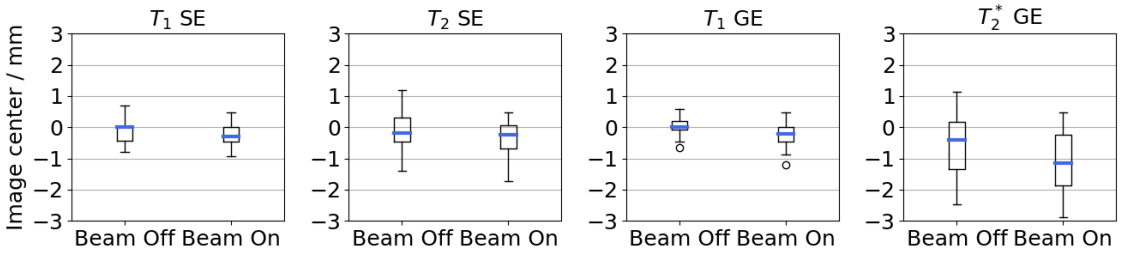

Fig. 8. Measured positions of the phantom center in FE (vertical) direction in MR images for the four different sequences, acquired with and without simultaneous irradiation.

field oscillation on the order of ±1.4 μT (±60 Hz), which was shown to correlate with ambient temperature, thus indicating imperfections in the thermic insulation of the temperature-sensitive permanent magnet material. Secondly, the operation of the proton beamline system resulted in a change in B_0 field strength on the order of 0.35 μT (15 Hz) induced by the fringe fields of the beamline magnets. Both of these effects may be compensated by the implementation of a more accurate f_0 calibration method directly before acquisition of each MR image [25]. Alternative measures to reduce these effects are an improvement in thermic insulation and magnetic shielding of the MR system against external fields, respectively. The image quality of our *in-beam* MR scanner was shown to be acceptable both with and without simultaneous proton beam irradiation. All geometrical parameters agreed with the physical dimensions of the ACR phantom within one pixel width, and most ACR image quality parameters were shown to be equivalent with and without simultaneous irradiation. However, as is common for low-field MR scanners when there is no averaging over multiple excitations, as is the case with the ACR protocol, the SNR was low. This resulted in a low image intensity uniformity and a high percentage signal ghosting ratio in comparison to the ACR Recommended Action Criteria. Furthermore, a fluctuation in the absolute phantom position accuracy in FE direction was observed, with an interquartile range of up to 1.5 mm. This effect can be understood by the accuracy of the pre-scan f_0 calibration method currently used by the MR imager, which is on the order of 50 Hz [26]. Hence, an error in the resonance frequency, Δf_0 , results in a spatial off-resonance misencoding $\Delta x = \Delta f_0/\gamma G_x$ in the frequency encoding direction, where γ is the gyromagnetic ratio of hydrogen nuclei (42.6 MHz/T) and G_x is the frequency encode gradient amplitude. For Δf_0 = 50 Hz and G_x = 0.7 mT/m for the T_2^*-weighted GE sequence this results in a calculated image shift of 1.7 mm, which corresponds with the observed interquartile range of 1.5 mm. As discussed above, this effect should ideally be corrected by the implementation of a more accurate f_0 calibration performed before each image acquisition. Alternatively, an absolute positioning technique in which the imaging object relative to a fixed reference frame or fiducial markers is visualized could be used to detect the apparent displacement of the magnetic isocenter relative to the proton beam. The phantom's median horizontal position showed a constant deviation of 1.6 mm from the center of the FOV for all acquisitions and all sequences (Fig. 8). This offset is systematic and showed a small interquartile range of $\leq$ 0.5 mm and thus can be attributed to manufacturing tolerances in the phantom holder design.

A statistically significant influence of simultaneous irradiation during image acquisition was observed as a decrease in the SNR and an apparent shift in the vertical position of the phantom. While the median decrease of 1.5 in SNR is not considered relevant, this effect can be tracked back to induced currents in the MR receiver coil due to irradiation [27], [28]. In contrast to the minor reduction in SNR, the sequence-dependent vertical shift of the phantom position showing median differences of up to 0.7 mm, which are due to changes in f_0 resulting from the beamline magnets' fringe fields, has to be addressed in future studies, as discussed above. While changes in f_0 generally affect the slice encoding direction in the same manner as the frequency encoding direction, the slice encoding gradient amplitude was larger than the FE gradient amplitude for all sequences. Hence, the slice position was less sensitive to B_0 field perturbations and showed median differences $<$ 0.2 mm in images acquired with and without simultaneous, which are considered to be within tolerance. The PE direction is generally not affected by uniform B_0 field changes and therefore showed no relevant changes ($\leq$ 0.2 mm). As the magnitude of the FE gradient is the smallest for the T_2^*-weighted GE sequence out of the four sequences studied, the effect of B_0 inhomogeneities was expected to be most prominent for this sequences. This was confirmed by the non-uniform distortions of the phantom from its circular shape that induced uncertainties to the Hough transform (Fig. 3). This study is subject to a number of limitations that arise from the particular setup. Firstly, the magnetic field gradient magnitudes of the MR pulse sequences used in this study were relatively small compared to those available on modern low-field-strength MRI systems equipped with high-performance gradient subsystems and advanced imaging methods [29], [30]. Therefore, it is expected that sequences with greater gradient amplitudes, and hence higher receiver bandwidths, will be more robust against geometric deformations, as voxel displacement is inversely proportional to gradient amplitude. Secondly, the MR imager features a relatively high magnetic field inhomogeneity, which limited the range of applicable sequences to standard SE and GE imaging. Commonly used alternatives for low-field-strength scanners featuring a much better field homogeneity, especially in the context of cine imaging for MR-guided radiation therapy and cardiac studies

are balanced steady state free precession (bSSFP) sequences, which have an intrinsically high SNR [31], [32]. However, bSSFP type sequences were not available on the MR system used in the current study. Thirdly, this study does not include a three-dimensional geometric distortion analysis, as was suggested by [8]. The reasons are twofold: (1) the MRI system used is considered a research prototype and the high magnetic field inhomogeneity would deem such an analysis to be challenging, and (2) to our knowledge no validated 3D distortion phantom exists that would fit into the knee coil used in this study. However, for a next generation clinical MRiPT prototype system, featuring a larger field-of-view and better magnetic field homogeneity, such an analysis should be included in the QA protocol. A fourth limitation of this study is that no dynamic effects of external magnetic field perturbations were investigated, such as a change in the magnetic fringe fields caused by switching on/off the nearby cyclotron or those of the proton beamline magnets during MR image acquisition. The former effects are known to potentially lead to severe image blurring [33], whereas the latter were recently reported to cause severe loss of image quality in the case of active proton pencil beam scanning without magnetic decoupling between the proton beam delivery system and the MRI system [34]. Furthermore, MR imaging performance characterization studies for MR-IGRT systems have been largely based on diagnostic guidelines from ACR and NEMA. However, standardized acceptance and QA criteria for MR-IGRT systems are still lacking in the literature. Such criteria need to incorporate the specific image quality requirements that result from therapeutic applications such as e.g. target localization, tissue segmentation, beam gating or target volume tracking. The AAPM Task Group 284 is currently working on recommendations for MR simulation in radiotherapy and the optimization of radiation therapy-specific MR workflows. However, for MRiPT we assume that additional recommendations will be required to account for the increased geometrical sensitivity that is inherent to proton therapy.

V. Conclusion

The imaging performance of a low-field *in-beam* MR scanner was characterized in the presence of magnetic fringe fields of a static proton research beamline. The results provide a first quantitative assessment of magnetic fringe field effects on the static magnetic field and image quality of the *in-beam* MR scanner during simultaneous proton beam irradiation. The MR images showed acceptable geometric quality with limitations typical for the particular low-field MRI system. The results of this study emphasize that monitoring the absolute geometric position of the MR images should be added to any future QA protocol for MRiPT systems.

Acknowledgment

The authors thank Layla Riemann for her contribution in both planning and performing the magnetometry experiments, Andrea Serra (ASG Superconductors S.p.A., Genova, Italy) for information and support regarding the MR image acquisition and Julien Smeets and Erik van der Kraaij (Ion Beam Applications SA, Louvain-la-Neuve, Belgium) for research and technical support.

References

[1] S. Acharya, B. W. Fischer-Valuck, R. Kashani, P. Parikh, D. Yang, T. Zhao, O. Green, O. Wooten, H. H. Li, Y. Hu, V. Rodriguez, L. Olsen, C. Robinson, J. Michalski, S. Mutic, and J. Olsen, "Online magnetic resonance image guided adaptive radiation therapy: First clinical applications," *International Journal of Radiation Oncology Biology Physics*, vol. 94, no. 2, pp. 394–403, Feb. 2016.

[2] B. W. Raaymakers, I. M. Jürgenliemk-Schulz, G. H. Bol, M. Glitzner, A. N. T. J. Kotte, B. van Asselen, J. C. J. de Boer, J. J. Bluemink, S. L. Hackett, M. A. Moerland, S. J. Woodings, J. W. H. Wolthaus, H. M. van Zijp, M. E. P. Philippens, R. Tijssen, J. G. M. Kok, E. N. de Groot-van Breugel, I. Kiekebosch, L. T. C. Meijers, C. N. Nomden, G. G. Sikkes, P. A. H. Doornaert, W. S. C. Eppinga, N. Kasperts, L. G. W. Kerkmeijer, J. H. A. Tersteeg, K. J. Brown, B. Pais, P. Woodhead, and J. J. W. Lagendijk, "First patients treated with a 1.5 T MRI-linac: clinical proof of concept of a high-precision, high-field MRI guided radiotherapy treatment," *Physics in Medicine & Biology*, vol. 62, no. 23, pp. L41–L50, Nov. 2017.

[3] G. P. Liney, B. Dong, E. Weber, R. Rai, A. Destruel, R. Garcia-Alvarez, D. J. Manton, U. Jelen, K. Zhang, M. Barton, P. Keall, and S. Crozier, "Imaging performance of a dedicated radiation transparent RF coil on a 1.0 Tesla inline MRI-linac," *Physics in Medicine & Biology*, vol. 63, no. 13, p. 135005, Jun. 2018.

[4] S. Y. Tari, K. Wachowicz, and B. G. Fallone, "A non-axial superconducting magnet design for optimized patient access and minimal SAD for use in a linac-MR hybrid: proof of concept," *Physics in Medicine and Biology*, vol. 62, no. 8, pp. N147–N160, Mar. 2017.

[5] B. M. Oborn, S. Dowdell, P. E. Metcalfe, S. Crozier, R. Mohan, and P. J. Keall, "Future of medical physics: Real-time MRI-guided proton therapy," *Medical Physics*, vol. 44, no. 8, pp. e77–e90, jul 2017.

[6] A. Hoffmann, B. Oborn, M. Moteabbed, S. Yan, T. Bortfeld, A. Knopf, H. Fuchs, D. Georg, J. Seco, M. F. Spadea, O. Jäkel, C. Kurz, and K. Parodi, "MR-guided proton therapy: a review and a preview," *Radiation Oncology*, vol. 15, no. 1, May 2020.

[7] S. M. Schellhammer, A. L. Hoffmann, S. Gantz, J. Smeets, E. van der Kraaij, S. Quets, S. Pieck, L. Karsch, and J. Pawelke, "Integrating a low-field open MR scanner with a static proton research beam line: proof of concept," *Physics in Medicine & Biology*, vol. 63, no. 23, p. 23LT01, Nov. 2018.

[8] Y. Hu, L. Rankine, O. L. Green, R. Kashani, H. H. Li, H. Li, R. Nana, V. Rodriguez, L. Santanam, S. Shvartsman, J. Victoria, H. O. Wooten, J. F. Dempsey, and S. Mutic, "Characterization of the onboard imaging unit for the first clinical magnetic resonance image guided radiation therapy system," *Medical Physics*, vol. 42, no. 10, pp. 5828–5837, Sep. 2015.

[9] S. Stapf and S.-I. Han, Eds., *NMR Imaging in Chemical Engineering*. Wiley, Dec. 2005.

[10] Hitachi, *Neodymium-Iron-Boron Magnets NEOMAX Magnetic Characteristics*, Hitachi Metals, Ltd., 2019.

[11] K. Kose and T. Haishi, "High resolution NMR imaging using a high field yokeless permanent magnet," *Magnetic Resonance in Medical Sciences*, vol. 10, no. 3, pp. 159–167, 2011.

[12] American College of Radiology, *Phantom Test Guidance of Use of the Small MRI Phantom for the MRI Accreditation Program*, Apr. 2018, retrieved April 17, 2018.

[13] G. B. Chavhan, P. S. Babyn, B. Thomas, M. M. Shroff, and E. M. Haacke, "Principles, Techniques, and Applications of T_2^*-based MR Imaging and its special applications," *RadioGraphics*, vol. 29, no. 5, pp. 1433–1449, Sep. 2009.

[14] M. Davids, F. G. Zöllner, M. Ruttorf, F. Nees, H. Flor, G. Schumann, and L. R. Schad, "Fully-automated quality assurance in multi-center studies using MRI phantom measurements," *Magnetic Resonance Imaging*, vol. 32, no. 6, pp. 771–780, Jul. 2014.

[15] L. Dünger, *Entwicklung und Etablierung der automatisierten Qualitätssicherung für Magnetresonanztomographie in der bildgestützten Strahlentherapie*, Technische Universität Ilmenau, BA thesis, 2017.

[16] R. O. Duda and P. E. Hart, "Use of the Hough transformation to detect lines and curves in pictures," *Communications of the ACM*, vol. 15, no. 1, pp. 11–15, Jan. 1972.

[17] J. Sun, M. Barnes, J. Dowling, F. Menk, P. Stanwell, and P. B. Greer, "An open source automatic quality assurance (OSAQA) tool for the ACR MRI phantom," *Australasian Physical & Engineering Sciences in Medicine*, vol. 38, no. 1, pp. 39–46, Nov. 2014.
[18] E. Walker and A. S. Nowacki, "Understanding equivalence and noninferiority testing," *Journal of General Internal Medicine*, vol. 26, no. 2, pp. 192–196, Sep. 2010.
[19] D. Lakens, "Equivalence tests," *Social Psychological and Personality Science*, vol. 8, no. 4, pp. 355–362, May 2017.
[20] S. Holm, "A simple sequentially rejective multiple test procedure," *Scand. J. Stat.*, vol. 6, no. 2, pp. 65–70, 1979.
[21] H. M. Gach, A. N. Curcuru, E. J. Wittland, B. Maraghechi, B. Cai, S. Mutic, and O. L. Green, "MRI quality control for low-field MR-IGRT systems: Lessons learned," *Journal of Applied Clinical Medical Physics*, vol. 20, no. 10, pp. 53–66, Sep. 2019.
[22] R. H. Tijssen, M. E. Philippens, E. S. Paulson, M. Glitzner, B. Chugh, A. Wetscherek, M. Dubec, J. Wang, and U. A. van der Heide, "MRI commissioning of 1.5T MR-linac systems – a multi-institutional study," *Radiotherapy and Oncology*, vol. 132, pp. 114–120, Mar. 2019.
[23] M. Blasche and D. Fischer, "Magnet Homogeneity and Shimming," Siemens Healthcare GmbH, Tech. Rep., 2017.
[24] J. P. Marques, F. F. Simonis, and A. G. Webb, "Low-field MRI: An MR physics perspective," *Journal of Magnetic Resonance Imaging*, vol. 49, no. 6, pp. 1528–1542, Jan. 2019.
[25] J. K. Maier, "Automatic RF frequency adjustment for magnetic resonance scanner," US Patent 4,806,866, 1989.
[26] A. Serra, Private Communication, 2018, ASG Superconductors S.p.A., Genoa, Italy.
[27] B. Burke, B. G. Fallone, and S. Rathee, "Radiation induced currents in MRI RF coils: application to linac/MRI integration," *Physics in Medicine and Biology*, vol. 55, no. 3, pp. 735–746, Jan. 2010.
[28] B. Burke, A. Ghila, B. G. Fallone, and S. Rathee, "Radiation induced current in the RF coils of integrated linac-MR systems: The effect of buildup and magnetic field," *Medical Physics*, vol. 39, no. 8, pp. 5004–5014, Jul. 2012.
[29] S. Klüter, "Technical design and concept of a 0.35 T MR-linac," *Clinical and Translational Radiation Oncology*, vol. 18, pp. 98–101, Sep. 2019.
[30] A. E. Campbell-Washburn, R. Ramasawmy, M. C. Restivo, I. Bhattacharya, B. Basar, D. A. Herzka, M. S. Hansen, T. Rogers, W. P. Bandettini, D. R. McGuirt, C. Mancini, D. Grodzki, R. Schneider, W. Majeed, H. Bhat, H. Xue, J. Moss, A. A. Malayeri, E. C. Jones, A. P. Koretsky, P. Kellman, M. Y. Chen, R. J. Lederman, and R. S. Balaban, "Opportunities in interventional and diagnostic imaging by using high-performance low-field-strength MRI," *Radiology*, vol. 293, no. 2, pp. 384–393, Nov. 2019.
[31] S. Rashid, F. Han, Y. Gao, K. Sung, M. Cao, Y. Yang, and P. Hu, "Cardiac balanced steady-state free precession MRI at 0.35 T: a comparison study with 1.5 T," *Quantitative Imaging in Medicine and Surgery*, vol. 8, no. 7, pp. 627–636, Aug. 2018.
[32] O. P. Simonetti and R. Ahmad, "Low-field cardiac magnetic resonance imaging," *Circulation: Cardiovascular Imaging*, vol. 10, no. 6, Jun. 2017.
[33] M. B. M. Hofman, J. P. A. Kuijer, J. W. de Ridder, L. R. Perk, and R. M. Verdaasdonk, "Technical note: Building a combined cyclotron and MRI facility: Implications for interference," *Medical Physics*, vol. 40, no. 1, p. 012303, Jan. 2013.
[34] S. Gantz, V. Hietschold, and A. L. Hoffmann, "Characterization of magnetic interference and image artefacts during simultaneous in-beam MR imaging and proton pencil beam scanning," *Physics in Medicine & Biology*, Aug. 2020.

APPENDIX A
MAGNETIC FIELD DRIFT

Figure A.1 shows the results of the drift measurement of the mean resonance frequency f_{16}, the MFH_{16} and the ambient temperature T_a over 4 days. The mean frequency (upper plot, solid blue line) follows an oscillating daily seasonality being negatively correlated (p = -0.62) to the room temperature change (upper plot, overlaid dashed black line). Sharp drops in the frequency indicate activities in the nearby treatment room (Influences of the treatment room on the B_0 field of the MR scanner were studied in detail but are beyond the scope of this work). Energized beamline magnets to the treatment room lead to a decreased frequency on the order of 20–30 Hz (results not shown in this study). The 2 h data-void on the second day corresponds to the time point of reference rotation measurements. The same trend is visible for MFH_{16} (lower plot), however the amplitude of the oscillation measures 1.5 ppm only.

APPENDIX B
IMAGE QUALITY PARAMETERS

The image quality parameters measured with and without simultaneous irradiation for the T_1- and T_2-weighted SE sequence, the T_1- and T_2^*-weighted GE sequence and the locator sequence, are given in the Tables B.1 to B.5, respectively.

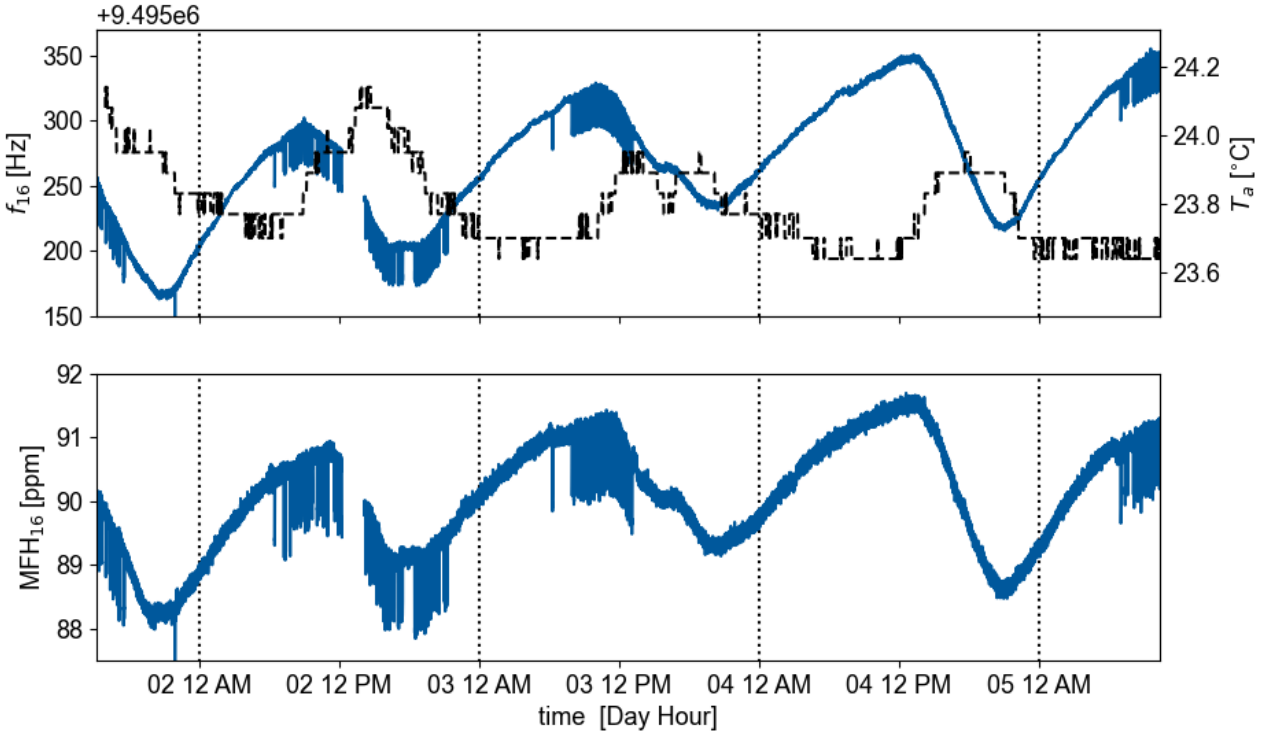

Fig. A.1. Multi-day drift measurement of the frequency (blue solid) and room temperature (black dashed) in the upper plot, as well as magnetic field homogeneity in the lower plot. Dotted vertical lines separate individual days. During the 2h data void on the second day reference rotation measurements were performed.

TABLE B.1
IMAGE QUALITY PARAMETERS FOR T_1-WEIGHTED SE SEQUENCE. STATISTICALLY EQUIVALENT PARAMETERS ARE MARKED BY ^{eq}. STATISTICALLY SIGNIFICANT DIFFERENCES ARE MARKED BY AN ASTERISK (*).

	ACR Recommended Action Criterion	Without irradiation median (interquartile range)		During irradiation median (interquartile range)		Difference of medians	
Phantom diameter in slice 1 / mm	100 ± 2	99.8	(99.7 to 100)	99.9	(99.8 to 100)	< 0.1	^{eq}
Phantom diameter in slice 3 / mm	100 ± 2	100	(100 to 100)	100	(100 to 100)	0.1	^{eq}
Horizontal phantom center / mm		1.6	(1.4 to 1.9)	1.4	(1.4 to 1.8)	0.2	^{eq}
Vertical phantom center / mm		0	(-0.5 to 0.0)	-0.3	(-0.5 to 0.0)	0.3	^{eq}
Slice position error / mm	≤ 4	0.8	(0.2 to 1.4)	0.9	(0.3 to 1.4)	-0.2	^{eq}
Slice thickness / mm	5.0 ± 0.7	5.4	(5.2 to 5.6)	5.5	(5.2 to 5.6)	-0.1	^{eq}
Resolution horizontal / mm	≤ 0.8	0.7	(0.7 to 0.7)	0.7	(0.7 to 0.7)	0	^{eq}
Resolution vertical / mm	≤ 0.8	0.7	(0.7 to 0.7)	0.7	(0.7 to 0.7)	0	^{eq}
SNR		45.4	(45.0 to 46.3)	44.8	(43.7 to 46)	0.6	^{eq,*}
Image Intensity Uniformity	≥ 87.5	83.2	(82.9 to 83.7)	83.1	(82.3 to 83.5)	0.1	^{eq}
Ghosting Ratio	≤ 0.025	0.054	(0.053 to 0.057)	0.055	(0.053 to 0.056)	-0.001	^{eq}
Number of detected low-contrast spokes	≥ 9	13	(10 to 13)	12	(11 to 13)	1	^{eq}

TABLE B.2
IMAGE QUALITY PARAMETERS FOR T_2-WEIGHTED SE SEQUENCE. STATISTICALLY EQUIVALENT PARAMETERS ARE MARKED BY $^{\text{eq}}$. STATISTICALLY SIGNIFICANT DIFFERENCES ARE MARKED BY AN ASTERISK (*).

	ACR Recommended Action Criterion	Without irradiation median (interquartile range)		During irradiation median (interquartile range)		Difference of medians	
Phantom diameter in slice 1 / mm	100 ± 2	99.8	(99.7 to 100)	99.8	(99.6 to 99.9)	< 0.1	$^{\text{eq}}$
Phantom diameter in slice 3 / mm	100 ± 2	100	(100 to 100)	100	(99.9 to 100)	< 0.1	$^{\text{eq}}$
Horizontal phantom center / mm		1.6	(1.4 to 1.9)	1.6	(1.4 to 1.9)	< 0.1	$^{\text{eq}}$
Vertical phantom center / mm		-0.2	(-0.5 to 0.3)	-0.2	(-0.7 to 0.1)	< 0.1	
Slice position error / mm	≤ 4	0.9	(0.4 to 1.4)	0.9	(0.4 to 1.3)	< 0.1	$^{\text{eq}}$
Slice thickness / mm	5.0 ± 0.7	4.8	(4.7 to 5.0)	4.8	(4.7 to 4.9)	< 0.1	$^{\text{eq}}$
Resolution horizontal / mm	≤ 0.8	0.7	(0.7 to 0.7)	0.7	(0.7 to 0.7)	0	$^{\text{eq}}$
Resolution vertical / mm	≤ 0.8	0.7	(0.7 to 0.7)	0.7	(0.7 to 0.7)	0	$^{\text{eq}}$
SNR		47.3	(46.6 to 47.6)	46.4	(45.6 to 47.1)	0.9	$^{\text{eq},*}$
Image Intensity Uniformity	≥ 87.5	76.5	(75.9 to 77.1)	76.2	(75.7 to 76.9)	0.3	$^{\text{eq}}$
Ghosting Ratio	≤ 0.025	0.044	(0.037 to 0.050)	0.045	(0.036 to 0.052)	-0.001	
Number of detected low-contrast spokes	≥ 9	11	(10 to 12)	10	(9 to 12)	1	$^{\text{eq}}$

TABLE B.3
IMAGE QUALITY PARAMETERS FOR T_1-WEIGHTED GE SEQUENCE. STATISTICALLY EQUIVALENT PARAMETERS ARE MARKED BY $^{\text{eq}}$. STATISTICALLY SIGNIFICANT DIFFERENCES ARE MARKED BY AN ASTERISK (*).

	ACR Recommended Action Criterion	Without irradiation median (interquartile range)		During irradiation median (interquartile range)		Difference of medians	
Phantom diameter in slice 1 / mm	100 ± 2	99.8	(99.7 to 99.8)	99.7	(99.5 to 99.8)	< 0.1	$^{\text{eq}}$
Phantom diameter in slice 3 / mm	100 ± 2	99.9	(99.8 to 100)	99.9	(99.7 to 100)	< 0.1	$^{\text{eq}}$
Horizontal phantom center / mm		1.6	(1.4 to 1.9)	1.4	(1.3 to 1.7)	0.2	$^{\text{eq}}$
Vertical phantom center / mm		0	(-0.1 to 0.2)	-0.2	(-0.5 to 0)	0.2	$^{\text{eq},*}$
Slice position error / mm	≤ 4	0.4	(-0.1 to 1.0)	0.3	(-0.2 to 0.6)	0.1	$^{\text{eq}}$
Resolution horizontal / mm	≤ 0.8	0.8	(0.8 to 0.8)	0.8	(0.8 to 0.8)	0	$^{\text{eq}}$
Resolution vertical / mm	≤ 0.8	0.8	(0.7 to 0.8)	0.8	(0.8 to 0.8)	0	$^{\text{eq}}$
SNR		14.2	(13.3 to 15.3)	13.4	(12.6 to 14.3)	0.8	$^{\text{eq}}$
Image Intensity Uniformity	≥ 87.5	88.0	(83.8 to 92.7)	86.0	(83.9 to 94.5)	2.0	$^{\text{eq}}$
Ghosting Ratio	≤ 0.025	0.016	(0.013 to 0.019)	0.015	(0.013 to 0.017)	< 0.001	$^{\text{eq}}$
Number of detected low-contrast spokes	≥ 9	0	(0 to 0)	0	(0 to 0)	0	$^{\text{eq}}$

TABLE B.4
IMAGE QUALITY PARAMETERS FOR T_2^*-WEIGHTED GE SEQUENCE. STATISTICALLY EQUIVALENT PARAMETERS ARE MARKED BY $^{\text{eq}}$. STATISTICALLY SIGNIFICANT DIFFERENCES ARE MARKED BY AN ASTERISK (*).

	ACR Recommended Action Criterion	Without irradiation median (interquartile range)		During irradiation median (interquartile range)		Difference of medians	
Phantom diameter in slice 1 / mm	100 ± 2	99.9	(99.6 to 100)	99.9	(99.7 to 100)	< 0.1	$^{\text{eq}}$
Phantom diameter in slice 3 / mm	100 ± 2	100	(99.3 to 100)	100	(99.9 to 101)	< 0.1	
Horizontal phantom center / mm		1.9	(1.6 to 2.0)	1.9	(1.7 to 2.0)	< 0.1	$^{\text{eq}}$
Vertical phantom center / mm		-0.4	(-1.3 to 0.2)	-1.2	(-1.9 to -0.2)	0.7	
Slice position error / mm	≤ 4	0.8	(0 to 1.2)	0.9	(0.1 to 1.1)	< 0.1	$^{\text{eq}}$
Slice thickness / mm	5.0 ± 0.7	5.7	(5.5 to 5.9)	5.7	(5.4 to 5.9)	< 0.1	$^{\text{eq}}$
Resolution horizontal / mm	≤ 0.8	0.8	(0.8 to 0.8)	0.8	(0.8 to 0.8)	0	$^{\text{eq}}$
Resolution vertical / mm	≤ 0.8	0.8	(0.8 to 0.8)	0.8	(0.8 to 0.8)	0	$^{\text{eq}}$
SNR		53.2	(50.9 to 54.4)	51.7	(49.2 to 52.6)	1.5	*
Image Intensity Uniformity	≥ 87.5	82.8	(79.7 to 86.6)	82.6	(81.0 to 85.1)	0.2	$^{\text{eq}}$
Ghosting Ratio	≤ 0.025	0.097	(0.080 to 0.111)	0.092	(0.078 to 0.104)	0.006	
Number of detected low-contrast spokes	≥ 9	1	(1 to 2)	2	(1 to 3)	-1	$^{\text{eq}}$

TABLE B.5
IMAGE QUALITY PARAMETER FOR THE LOCATOR SE SEQUENCE. THE PHANTOM LENGTH WAS STATISTICALLY EQUIVALENT WITH AND WITHOUT IRRADIATION (AS INDICATED BY $^{\text{eq}}$).

	ACR Recommended Action Criterion	Without irradiation median (interquartile range)		During irradiation median (interquartile range)		Difference of medians	
Phantom Length / mm	100 ± 2	99.9	(99.8 to 100)	99.9	(99.8 to 100.1)	0	$^{\text{eq}}$